International Journal of Refractory Metals and Hard Materials 118 (2024) 106469

Contents lists available at ScienceDirect

International Journal of Refractory Metals and Hard Materials

journal homepage: www.elsevier.com/locate/IJRMHM

Promoted high-temperature strength and room-temperature plasticity synergy by tuning dendrite segregation in NbMoTaW refractory high-entropy alloy

Bo Sun [a], Qianqian Wang [a,b,*], Jinyong Mo [c], Bingjie Wang [a], Xiubing Liang [c], Baolong Shen [a,*]

[a] School of Materials Science and Engineering, Jiangsu Key Laboratory for Advanced Metallic Materials, Southeast University, Nanjing 211189, China
[b] School of Materials Science and Engineering, Jiangsu Key Laboratory of Advanced Structural Materials and Application Technology, Nanjing Institute of Technology, Nanjing 211167, China
[c] Defense Innovation Institute, Academy of Military Science, Beijing 100071, China

ARTICLE INFO

Keywords:
Refractory high-entropy alloy
Dendrite segregation
Heterostructure
Mechanical property
High temperature

ABSTRACT

NbMoTaW refractory high-entropy alloy (RHEA) exhibits high strength and excellent softening resistance at elevated temperature, while normal compositional modification cannot overcome the trade-off between high-temperature (HT) strength and room-temperature (RT) plasticity. Here, we proposed a heterostructure strategy by tuning dendrite segregation to reach large RT plasticity without deterioration in HT strength. The optimized $Nb_{45}Mo_{45}Ta_5W_5$ RHEA shows large RT plasticity of 6.1% and high yield strength of 440 MPa at 1873 K, which mainly originates from the heterostructure. Nanoscale precipitates form in the interdendrite region after annealing at 1873 K, which further increases the RT plasticity to 9.0% with a comparable yield strength of 415 MPa at 1873 K. The strength retention up to 1873 K arises from the large modulus misfit of $Nb_{45}Mo_{45}Ta_5W_5$ alloy and the hetero-deformation in the dendrite and interdendrite regions. The nanoscale precipitates in the interdendrite region is temperature-dependent and stress-promoted, which contributes to work-hardening at RT and softening resistance at 1873 K. The dendritic heterostructure strategy in this work provide a feasible method to toughen brittle RHEAs and paves the way to design RHEAs with excellent HT strength in combination of large RT plasticity.

1. Introduction

High strength and excellent resistance to high-temperature (HT) softening are essential for the application of structural materials at elevated temperature [1–3]. Owing to the high-entropy effect and sluggish diffusion that arising from the multi-principal mixture of high melting-temperature elements [4,5], refractory high-entropy alloys (RHEAs) exhibit excellent mechanical properties at HT. In 2010, NbMoTaW RHEA was reported with high compressive strength of 600 MPa at 1873 K and remarkable softening resistance above 1200 K [6,7]. In addition, it also exhibited outstanding structural stability even after annealing at 1373 K for 3 days [8]. In the past decade, NbMoTaW system RHEAs have attracted widespread attention and are considered as one of the most promising candidates for the next-generation HT-resistant materials [9–11].

Refractory elements also leave drawbacks to NbMoTaW RHEA, which mainly includes two aspects: i) the intrinsic brittleness with a fracture strain of only 2.1% at room temperature (RT) makes it virtually impossible for casting or machining [7]; ii) a high density of 13.75 g/cm^3 reduces the specific strength [6]. Recently, many efforts have been devoted to overcoming these dilemmas [12,13]. By alloying with ductile Ti element, Yao et al. found that the TiNbMoTaW RHEA inhibited fracture at RT until the compressed strain exceeded 14%, and accompanied with a reduced density of 11.85 g/cm^3 [14]. Unfortunately, the RHEA started to soften rapidly above 1073 K due to the relatively low melting temperature (T_m) of Ti, and the compressive strength of TiNbMoTaW RHEA retained only 173 MPa at 1873 K [15]. Adding Re (with high T_m of 3459 K) or replacing Nb by Re could also improve the RT strength and plasticity of NbMoTaW RHEA [16,17], but deteriorate HT strength. However, MoTaReW RHEA shows low structure stability at

* Corresponding authors at: School of Materials Science and Engineering, Jiangsu Key Laboratory for Advanced Metallic Materials, Southeast University, Nanjing 211189, China.
E-mail addresses: qwang678@seu.edu.cn (Q. Wang), blshen@seu.edu.cn (B. Shen).

https://doi.org/10.1016/j.ijrmhm.2023.106469
Received 25 August 2023; Received in revised form 21 October 2023; Accepted 1 November 2023
Available online 10 November 2023

grain boundary (GB) at 1873 K, and the trade-off between the HT strength and RT plasticity reappears [18]. These studies strongly suggest that the co-constrains between RT plasticity, HT strength and material density are difficult to resolve by simple compositional adjustment such as alloying or replacement of ductile elements.

Dendrite segregation is an inevitable structure to most RHEAs prepared by casting or additive manufacturing. For NbMoTaW RHEA, the high melting-point elements (W and Ta) usually solidify as dendrites whereas the Mo and Nb elements with relatively low T_m tend to segregate at the interdendrite region [6]. Such melting point-induced dendrite segregation is independent of the preparation methods, and becomes even more pronounced as the RHEA prepared by laser manufacturing technologies with faster solidification rates [19]. Dendrite segregation in RHEAs usually has high structural stability and is difficult to be homogenized by normal annealing treatment. It has been reported that CrVNbMo RHEA still remained dendrite segregation after annealing at 1273 K for 21 days [20]. Based on the large difference in T_m between the constituent elements, Lu et al. designed a dual-phase ZrNbMoTaW RHEA with excellent RT plasticity of >15% and low density of 12.25 g/cm^3 [21]. The outstanding RT plasticity mainly attributes to the strong heterogeneous hardening effect between the hard BCC1 dendrites and the soft BCC2 phase at the interdendrite. However, ZrNbMoTaW RHEA softened at 1273 K, as mentioned previously, due to the low T of Zr. For NbMoTaW RHEA, it also shows a large difference in the T_m between its constituent elements (~945 K) which offers possibility to be toughened by the heterostructure, but this has not received attention.

In this work, based on the intrinsic dendrite segregation behavior in RHEA, we proposed a heterogeneous strengthening strategy to overcome the trade-off between RT plasticity and HT strength in NbMoTaW RHEA. $Nb_xMo_xTa_{50-x}W_{50-x}$ (x = 5, 25, 45 at.%) RHEAs were designed by directly modifying the content of the segregated elements (Mo and Nb) at the interdendrite region. The RT strength and plasticity of $Nb_5Mo_5Ta_{50-x}W_{50-x}$ RHEA were simultaneously improved without obvious deterioration in yield strength at 1873 K, while the material density significantly decreased to 10.35 g/cm^3. The microstructure of the as-cast, annealed and HT-deformed $Nb_5Mo_5Ta_{50-x}W_{50-x}$ samples was detailly analyzed to reveal the underlying mechanisms for the structure evolution and excellent mechanical properties from RT to 1873 K. The dendrite segregation dominated heterostructure strengthening strategy is expected to be a simple and effective method to improve the comprehensive mechanical properties of brittle NbMoTaW system RHEAs in a wide temperature range.

2. Materials and methods

Ingots of $Nb_xMo_xTa_{50-x}W_{50-x}$ (x = 5, 25, 45 at. %) were prepared by vacuum arc melting using bulk metals (Nb, Mo, Ta, W) with high purity (≥ 99.95 wt%). Pure Ti was used as a getter to remove the residual oxgyen in the chamber. All of the ingots were prepared with a melting current of ~300 A, and remelted at least six times to ensure high chemical homogeneity. Annealing at 1873 K for 500 min was performed on the as-cast ingots with a same heating and cooling rates of ~10 K/s. The as-cast and annealed $Nb_xMo_xTa_{50-x}W_{50-x}$ (x = 5, 25, 45 at. %) samples were denoted as NMx-AC and NMx-AN (x = 5, 25, 45), respectively.

Phase structure was analyzed by X-ray diffraction (XRD, Bruker D8 Discover) with a scanning rate of 4°/min. Material density was measured by Archimedes method using NMx-AC samples. Microstructure analysis was performed via scanning electron microscope (SEM, FEI Nova Nano 450) equipped with back-scattering electron (BSE), electron back-scattering diffraction (EBSD, FEI Sirion) and transmission electron microscope (TEM, Talos F200X). SEM samples were polished by diamond polishing paste and etched in a mixed acid solution ($HCl:HNO_3$:$HF:H_2O$ = 3:1:1:1) for 30 s. EBSD tests were performed with a step size of 1 μm, and the results were analyzed by Channel 5 software. EBSD samples were polished by SiO_2 nano-suspension for 6 h using a vibratory polisher (Buehler Vibromet 2). TEM samples were cut from the medium of ingots and thinned by an ion-beam thinner (GATAN-M691). Nano-indentation tests were carried out at ambient temperature with NanoTest System (Micro Materials Ltd.). The interval, maximum load, dwell time was 30 μm, 20 mN, 10 s, respectively, and both the loading and unloading rates were 0.5 mN/s. Compression tests were conducted with a strain rate of 10^{-3} s^{-1} at RT and 1873 K on an Instron-5982 machine and Zwick-KAPPA100 machine, respectively. Cylinder samples with dimensions of Φ2 mm × 4 mm cut from the center of the ingots were used for compression tests.

Equilibrium phase diagrams of the NMx alloys were calculated using the Thermal-Calc software (version 2021a) with the TCHEA database (version 4.2) [22,23]. The single-crystal elastic constants of NMx alloys were calculated by the first-principal calculation with a combination of Vienna Ab-initio Simulation Package (VASP) method [24], projector augmented wave (PAW) method [25] and special quasi-random structures (SQSs) [26]. Besides, all the parameters for the first-principal calculation were the same as our previous work [27].

3. Results

3.1. Mechanical properties

Compressive mechanical properties of the NMx alloys are illustrated in Fig. 1, and the values of the yield strength, compression strength and peak strain at RT and 1873 K are summarized in Table 1 and Table 2, respectively. The strength and plasticity of NMx-AC samples are simultaneously improved as alloying with more Nb and Mo (Fig. 1a). NM45-AC sample obtains the highest compressive strength of 1460 MPa and the largest peak strain of 6.1%. The strength and plasticity of NMx-AN samples show a similar improvement with the increasing content of Nb and Mo, and NM45-AN sample exhibits the superior mechanical properties especially with an excellent peak strain of 9.0% (Fig. 1b). Obviously, the RT mechanical properties (especially the plasticity) of both the as-cast and annealed NM45 alloy are much better than the NbMoTaW RHEA (i.e., NM25 alloy). Fig. 1c shows the compressive stress-strain curves of NMx alloys at 1873 K. The yield strength and compression strength of NM25-AC sample is 497 MPa and 509 MPa, respectively, which is comparable as the reported results [7]. The NM45-AC and NM45-AN samples also have high yield strength >400 MPa, which is surprisingly comparable with that of NM25-AC sample. In comparison with other NbMoTaW system RHEAs [7,14,15,18,28,29], the yield strength at 1873 K vs. the peak strain at RT, as well as the specific yield strength at 1873 K vs. the homologous temperature, i.e., the ratio of testing temperature to the melting temperature (T/T_m), of NM45 alloy is plotted in Fig. 1d and e, respectively. Obviously, both the as-cast and annealed NM45 samples are strong at 1873 K and ductile at RT (Fig. 1d). Although the NbMoTaW RHEAs doping with metalloids B or C [29] show higher RT strength and larger plasticity at 1873 K (Fig. 1d), NM45 alloy performs better when material density and melting temperature are considered (Fig. 1e). It is necessary to lighten weight for the potential application towards some hot-end structural materials that used in extreme environment. Compared with other RHEAs, NM45 alloy has outstanding specific yield strength as tested at high homologous temperatures, which facilitates its application as HT structural materials with high servicing security.

Fig. 2 illustrates the fracture surface morphology of NMx-AC samples after the compression at RT. It shows intergranular fracture for NM5-AC sample while quasi-cleavage fracture for NM25-AC and NM45-AC samples. Notably, the NM45-AC sample shows smaller fracture facet with denser quasi-cleavage steps as compared with the NM25-AC sample, indicating NM45 alloy is more resistant to quick propagation of cracks. Fig. 3 exhibits the fracture surface of NMx samples after compression at 1873 K. All samples show material spallation from the side surface, as indicated by the red arrows, implying a sluggish failure

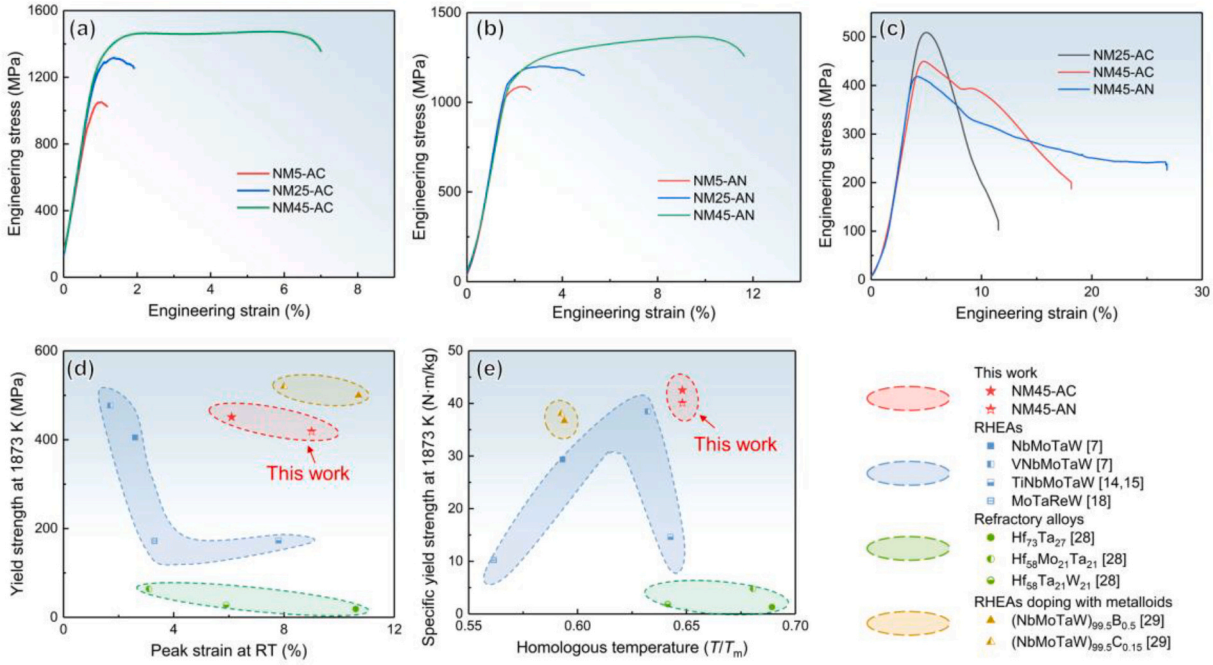

Fig. 1. **Fig. 1** Mechanical properties of NMx alloys. Compressive stress-strain curves at RT for (a) NMx-AC samples and (b) NMx-AN samples; (c) compressive stress-strain curves at 1873 K; comparison of (d) yield strength at 1873 K vs. peak strain at RT and (e) specific yield strength at 1873 K vs. homologous temperature between NM45 alloys and other materials.

Table 1
Compression properties of NMx alloys at RT.

RHEAs	Yield strength (MPa)	Compression strength (MPa)	Peak strain (%)
NM5-AC	1017 ± 49	1077 ± 34	1.3 ± 0.3
NM25-AC	1220 ± 47	1282 ± 66	2.1 ± 0.2
NM45-AC	1334 ± 32	1460 ± 24	6.1 ± 0.9
NM5-AN	927 ± 61	996 ± 151	1.2 ± 0.3
NM25-AN	1156 ± 114	1220 ± 205	1.6 ± 1.0
NM45-AN	1120 ± 23	1356 ± 25	9.0 ± 0.8
NbMoTaW [7]	1058	1211	1.5

Table 2
Compression properties of NMx alloys at 1873 K.

RHEAs	Yield strength (MPa)	Compression strength (MPa)
NM25-AC	497	509
NM45-AC	440	451
NM45-AN	415	419
NbMoTaW [7]	405	600

that corresponds to the strain softening stage in stress-strain curves.

3.2. Microstructure of the as-cast NMx alloys

Fig. 4 shows the equilibrium phase diagrams of NMx alloys and the XRD patterns of NMx-AC samples. In Fig. 4a, the phase diagrams predict a single body-centered cubic (BCC) phase in NM5, NM25 and NM45 alloys. The solidification temperature of NMx alloys gradually decreases with the increasing content of Mo and Nb. The solidification temperature range ΔT (T_{liquid}-T_{solid}) is 46 K, 60 K and 15 K for NM5, NM25 and NM45 alloys, respectively, implying all NMx alloys experience a rapid solidification process. All NMx-AC samples exhibit a single BCC phase in the XRD patterns (Fig. 4b), which is consistent with the prediction in equilibrium phase diagram (Fig. 4a). Table S1 lists the theoretical and experimental lattice constants of NMx alloys that predicted by the role-of-mixture method [30] and calculated by the XRD patterns of NMx-AC samples, respectively. The theoretical and experimental values are very close. Besides, the material densities of NMx alloys were predicted by the role-of-mixture method and measured by the Archimedes method, respectively, and given in Table S1. The theoretical and experimental density values are also similar for NMx alloys. It shows that increasing the content of Nb and Mo elements significantly decreases the density of the NMx RHEAs. NM45-AC sample has the lowest density of 10.35 g/cm^3.

Fig. 5 presents the BSE-SEM images and the EBSD orientation maps of NMx-AC samples. All of the NMx-AC samples are composed of nearly-equiaxed grains without obvious solidification microtexture. The average grain size is 95 μm, 104 μm and 96 μm for NM5-AC, NM25-AC and NM45-AC samples, respectively, indicating limited influence of the content of Nb and Mo elements on the grain size. Obvious dendrite segregation is visible inside the coarse grains in NM25-AC and NM45-AC samples, but not in NM5-AC sample. Besides, both BSE-SEM images and the orientation maps show straight GBs in NM5-AC sample while serrated GBs in NM25-AC and NM45-AC samples. The above differences (at GBs and within the coarse grains) indicate a changed solidification behavior with the increasing content of low melting-point elements Mo and Nb.

Fig. 6 presents the composition analysis by SEM-EDS for NMx-AC samples. The elemental content within the coarse grains in NM5-AC sample is close to its nominal value (Fig. 6a), while both the composition of dendrite (DR, as illustrated by the red arrows in Fig. 5b and c) and the interdendrite (ID, as illustrated by the blue arrows in Fig. 5b and c) deviates from the nominal composition in NM25-AC and NM45-AC samples. The segregation ratio of the elements at DR can be calculated by $K_i = c_i^{DR}/c_i^{ID}$ [6,31], where K_i, c_i^{DR} and c_i^{ID} represents the segregation ratio, the content at DR region and the content at ID region, respectively, for the element *i*. $K > 1$ indicates that the element *i* segregates in the DR region, and the more severe segregation the dendrites would have, the more the *K* value deviates from 1. As shown in Fig. 6b, the *K* values of W and Ta are higher than 1 for NM25-AC sample, indicating that these elements tend to segregate in dendrites. Despite W and Ta, the *K* value of

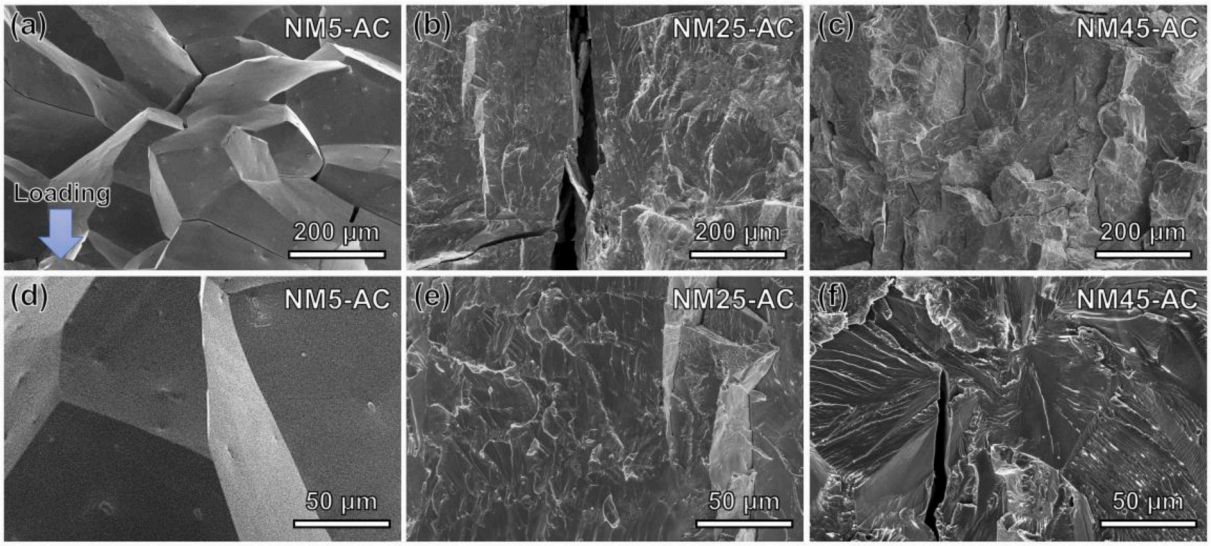

Fig. 2. **Fig. 2** Fracture surface of NMx-AC samples after compression at RT. (a, d) NM5-AC; (b, e) NM25-AC; (c, f) NM45-AC.

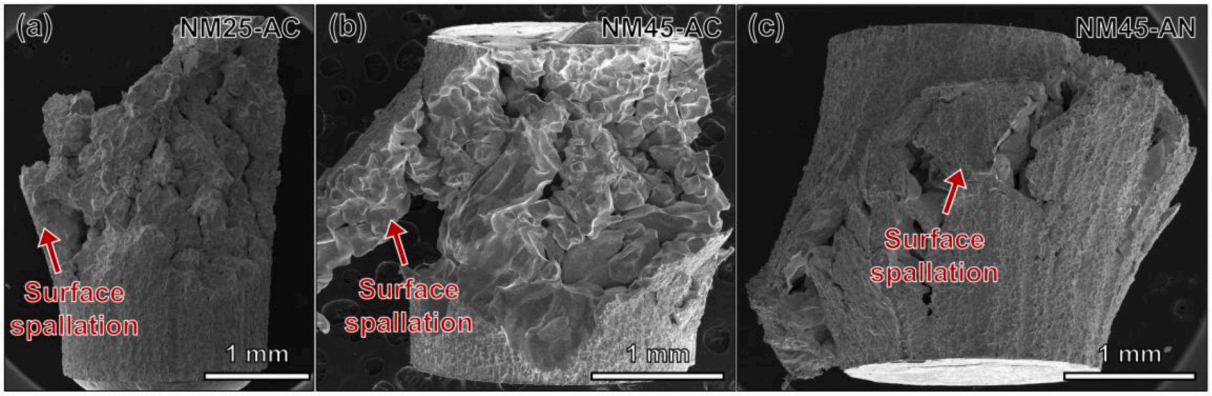

Fig. 3. **Fig. 3** Fracture surface of NMx samples after compression at 1873k. (a) NM25-AC; (b) NM45-AC; (c) NM45-AN.

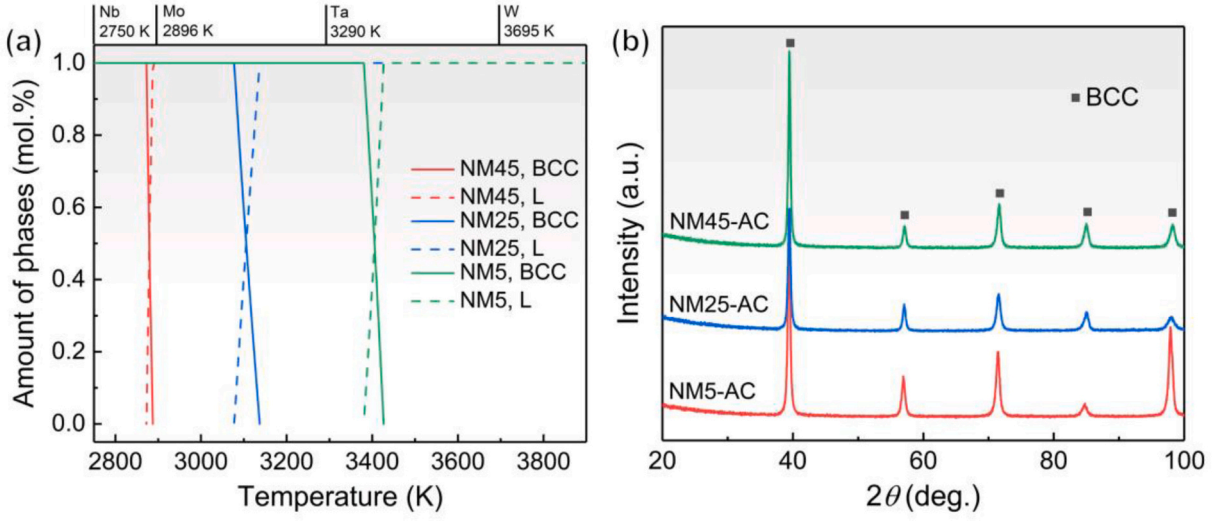

Fig. 4. **Fig. 4** (a) Equilibrium phase diagrams of NMx alloys; (b) XRD patterns of NMx-AC samples.

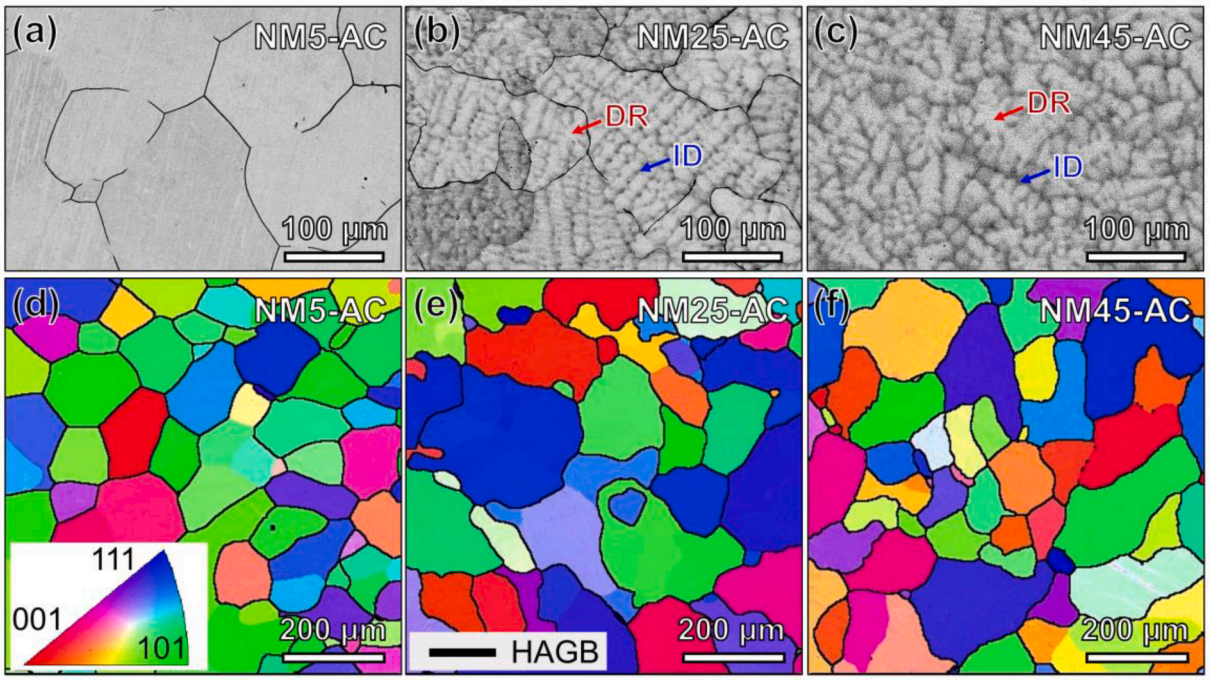

Fig. 5. **Fig. 5** (a–c) BSE-SEM images and (d–f) orientation maps with high-angle grain boundaries (HAGBs) of NMx-AC samples. (a, d) NM5-AC; (b, e) NM25-AC; (c, f) NM45-AC.

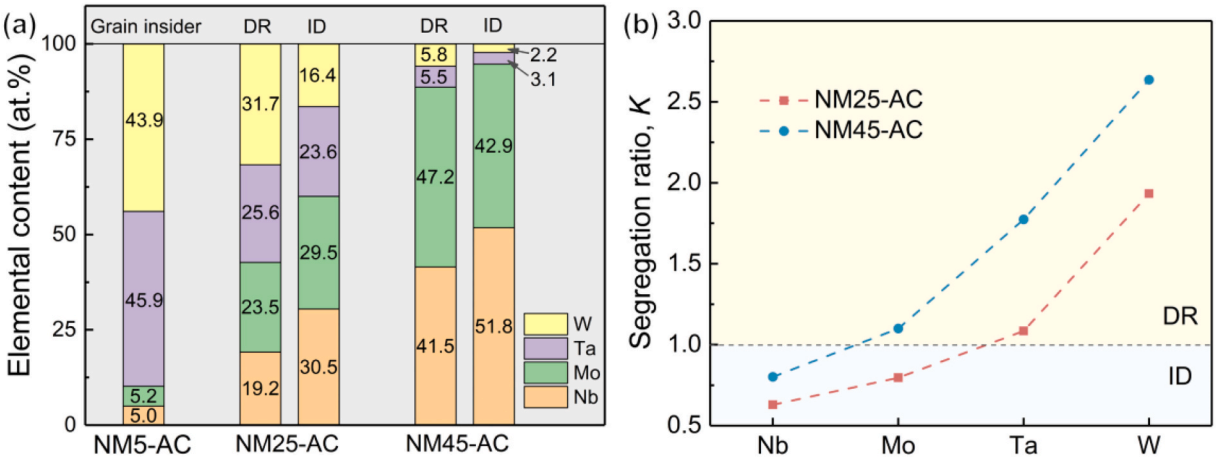

Fig. 6. **Fig. 6** (a) Elemental content and (b) segregation ratio of NMx-AC alloys.

Mo is also higher than 1 in NM45-AC sample, which suggests that both W, Ta and Mo are prone to form dendrites. The difference of the segregated elements within the dendrites also implies that the constituent elements of NM25 and NM45 alloys underwent dissimilar solidification behavior, which would be analyzed later.

Fig. 7 shows the dark field (DF) TEM images at the GBs of NMx-AC samples and their corresponding elemental distribution. NM5-AC sample shows a straight GB while a serrated GB is visible in NM25-AC and NM45-AC (Fig. 7a–c), which is in accordance with the SEM results. Notably, O segregation exists at GBs in all of the three samples, and can be defined as Ta—Nb rich oxides by the elemental distribution (Fig. 7d–f). The specific compositions at locations A–E (see Table S2) evidence that the oxide is discontinuously distributed with a multi-component composition. In addition, Fig. S1 shows the diffraction analysis of the NM45-AC sample, and it demonstrates that the oxide is indeed located at GBs rather than inside the grains.

3.3. *Microscale heterogeneity of the dendrite segregation*

The structural heterogeneity of the dendrite segregation was analyzed by nanoindentation tests. Fig. 8a, b show the cumulative curves of hardness and reduced modulus at the DR and ID regions for NM25-AC and NM45-AC samples, and the corresponding average values are present in Fig. 8c, d. Besides, the appearance of the nanoindentation at DR and ID is illustrated as the insets in Fig. 8a, b. The average size of the ID region and the indentation impression is 4.63 μm and 1.92 μm, respectively, for NM25-AC sample while 4.66 μm and 1.76 μm, respectively, for NM45-AC sample. Only the indentations that are entirely within DR region or located at ID region would be considered for comparison in this work. Both samples show higher hardness and lower reduced modulus at the ID region than the DR region, which confirms the dendrites in the coarse grains as heterostructure. For NM25-AC sample, the average values of hardness and reduced modulus are 6.84 GPa, 239.82 GPa and 7.35 GPa, 234.91 GPa in the DR and ID regions,

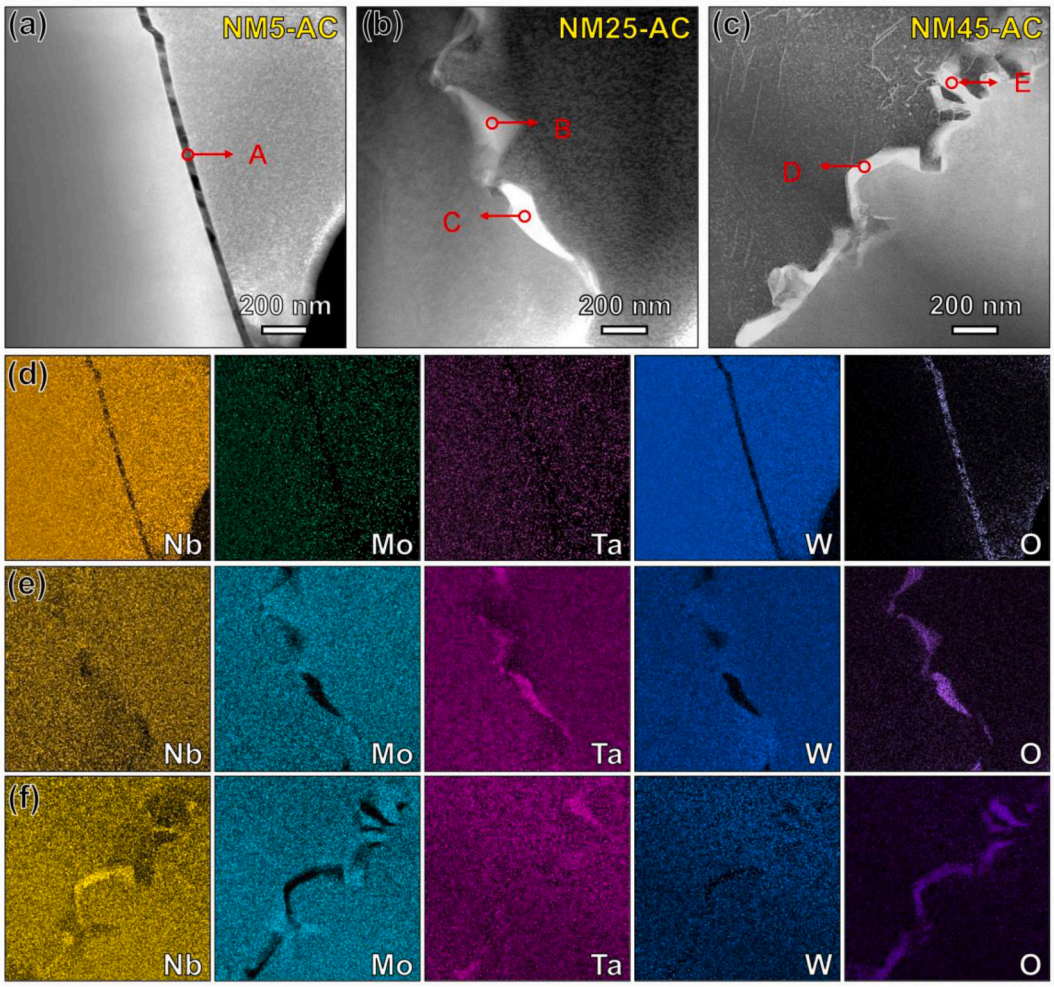

Fig. 7. Fig. 7 (a–c) Dark field (DF) images and (d–f) the corresponding elemental distribution of the NMx-AC samples. (a, d) NM5-AC; (b, e) NM25-AC; (c, f) NM45-AC.

respectively. For NM45-AC sample, the hardness is 6.60 GPa (DR) and 7.49 GPa (ID) while the reduced modulus is 235.95 GPa (DR) and 235.61 GPa (ID). High deviation in harness (0.89 GPa) together with small difference in reduced modulus (0.34 GPa) between the DR and ID regions suggest that NM45 alloy have a stronger heterogeneous strengthening effect accompanied with more coordinated deformation ability [32]. In addition, the average values of hardness and reduced modulus for NM25-AC sample are 7.01 GPa and 238.2 GPa, respectively, while the values for NM45-AC sample are 6.99 GPa and 235.8 GPa, respectively. This suggests NM45-AC sample has comparable hardness and modulus as compared with NM25-AC sample.

3.4. *Microstructure of the annealed NMx alloys*

Annealing treatment at 1873 K for 500 min was carried out to evaluate the structural stability of NMx alloys. As shown in Fig. 9, the XRD patterns of NMx-AN samples remain a single BCC structure, indicating that no other phases formed during the annealing process. The cross sections of the annealed samples were analyzed by BSE-SEM, as shown in Fig. 10. NM5-AN sample shows no obvious change after annealing treatment, i.e., equiaxed grains with straight GBs and no precipitate (Fig. 10a). NM25-AN sample shows the similar dendrite segregation with serrated GBs as NM25-AC sample, while a small amount of precipitates appear in the ID region, as indicated by the yellow arrows in Fig. 10b. NM45-AN sample also maintains the dendrite segregation and serrated GBs, but a large amount of precipitates is visible in the ID region (Fig. 10c). Closer observation shows that these precipitates show hole-like appearance after immersion in the mixed acid solution (Fig. 10d). The above results suggest that the microstructure of NM5 and NM25 alloys is stable at 1873 K, whereas the low structural stability in the ID region of NM45 alloy promotes the precipitation.

TEM observation was performed on NM-45AN sample to further analyze the microstructure of the precipitates. Fig. 11a illustrates two different appearances of the precipitates, i.e., the particle-like and the rod-shaped. The average diameter of the particle-like precipitates is 102 nm, while the average width of the rod-shaped precipitates is 105 nm. Particle-like precipitates tend to separate while most rod-shaped precipitates intersect with each other at specific angles, implying that the precipitation follows preferential orientations. Fig. 11b exhibits the high-resolution TEM (HRTEM) image at the phase boundary (PB) between the particle-like precipitate with the matrix. Fig. 11c–h show the inverse fast Fourier transform (IFFT) images and the fast Fourier transform (FFT) images of the matrix, the precipitate and the PB, respectively. The precipitate exhibits different lattice fringe with the matrix along the zone axis of $[\bar{1}11]_{BCC}$ but shows a coherent PB with the BCC matrix. The FFT image of the PB (Fig. 11h) firmly evidences that, the precipitate is a long-period stacking ordered structure and decomposes out from the disordered BCC matrix along the closely-packed $\{110\}_{BCC}$ planes. Besides, the atomic strain distribution images (Fig. 11i and j) show severer lattice distortion in the ordered precipitate than the matrix.

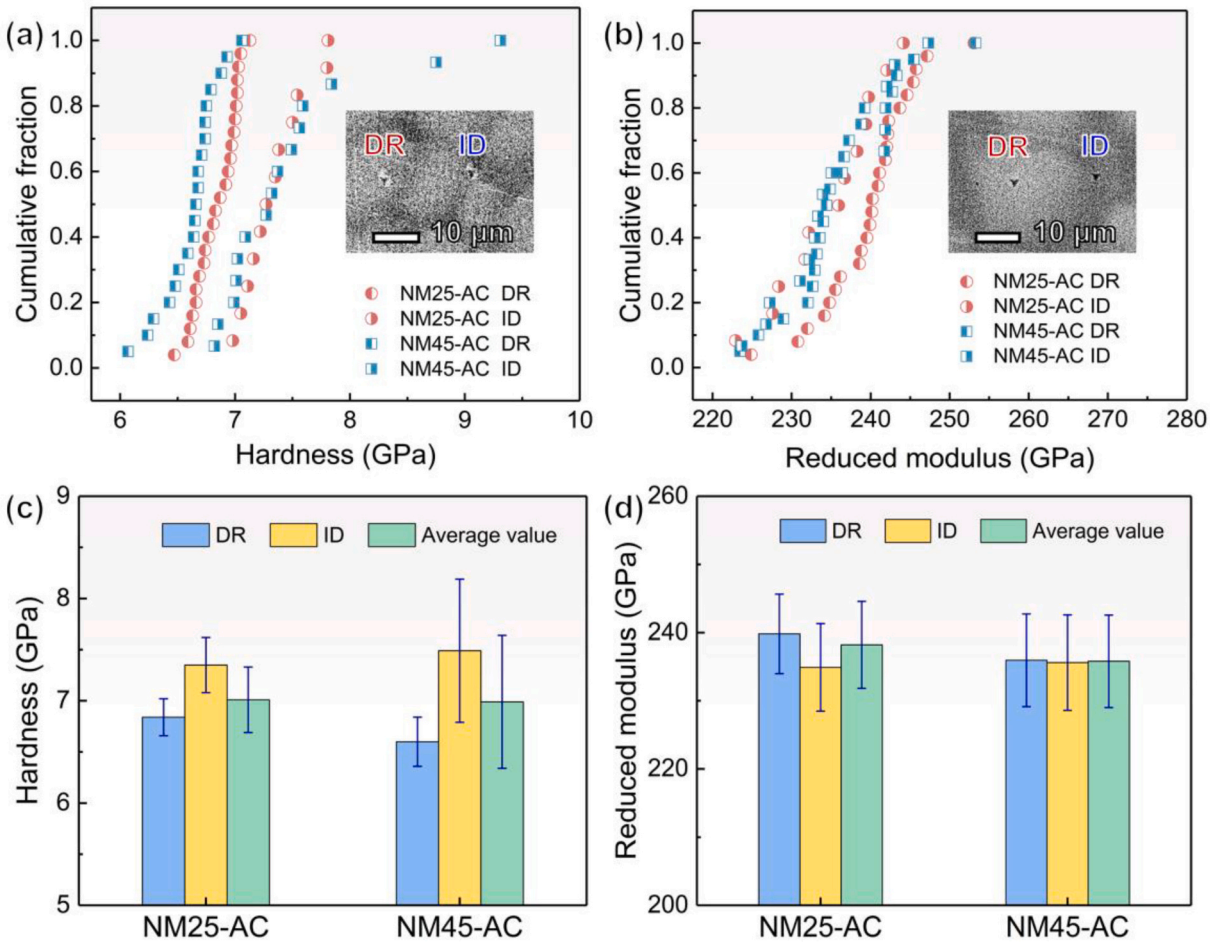

Fig. 8. Fig. 8 Nanoindentation analysis on structural heterogeneity for NM25-AC and NM45-AC samples. Cumulative curves of (a) hardness and (b) reduced modulus; the appearance of the nanoindentation is illustrated as the insets; average values of (c) hardness and (d) reduced modulus.

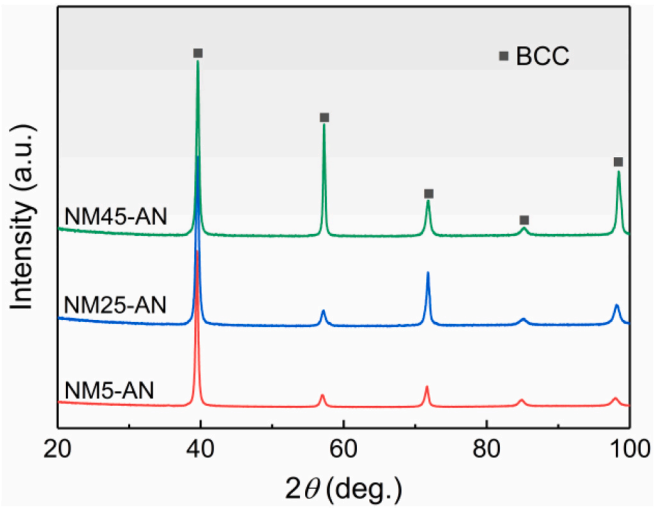

Fig. 9. Fig. 9 XRD patterns of NMx-AN samples.

Dislocations around the precipitates (Fig. 11a and Fig. 12a) are very different with that in the as-cast sample (Fig. 12b). The particle-like precipitates can pin the dislocations (see the orange indicators in Fig. 11a) and contribute to dislocation multiplication. Fig. 12a shows several intersected dislocations around the small rod-shaped precipitates (see the blue indicators), which is much distinctive with the dislocations in NM45-AC sample, implying that the growth of the rod-shaped precipitates may relate with the dislocation interactions. Fig. 12c presents the elemental maps, which demonstrates the decomposition of Nb and Ta elements out from the BCC matrix as the formation of precipitates. The specific compositions at locations F—H in Fig. 12c are given in Table S3. It shows that the contents of O, Ta and Nb in the matrix, the rod-shaped and particle-like precipitates gradually increase with the reduced contents of Mo and W.

3.5. *Microstructure of NMx alloys after compression at 1873 K*

Dissimilar with the Senkov's report [7], all NMx samples show a continuous drop of stress after yielding at 1873 K (Fig. 1c). To investigate the underlying mechanism, the cross-section morphology of NMx samples after compression at 1873 K was analyzed. As shown in Fig. 13a–c, coarse cracks appear in all of the NMx samples and they seem to tear and propagate along the HAGBs. Slim cracks were also visible in Fig. 13d–f. Nothing is noticeable around the HAGBs in NM25-AC sample. For NM45-AC sample, some precipitates appear in the ID region where cracks are separated, implying they can help to resist rapid failure. NM45-AN sample is more resistant to the propagation of cracks due to the existence of the large amount of precipitates at ID with less slim cracks, which is consistent with the slow softening rate in the stress-strain curve.

TEM analysis was conducted on NM45-AC sample after the deformation at 1873 K to uncover the origin for the excellent HT strength. In the DR region (Fig. 14a, b), multiplied dislocations are entangled with each other and gradually form low-angle grain boundaries (LAGBs, see

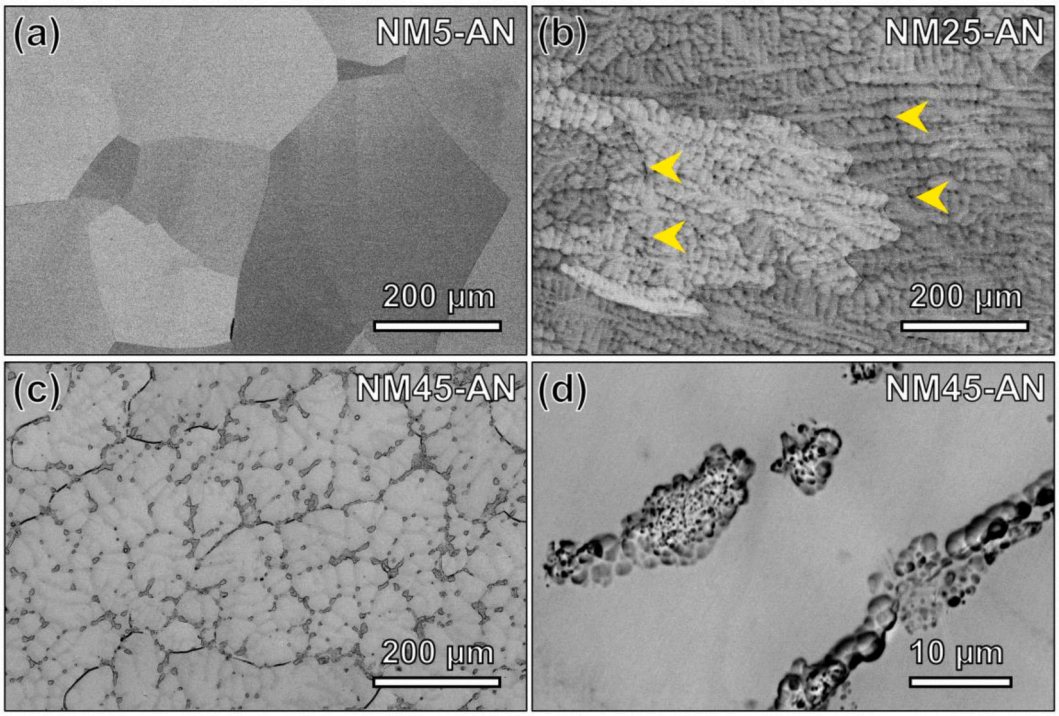

Fig. 10. Fig. 10 BSE-SEM images of NMx-AN samples. (a) NM5-AN; (b) NM25-AN; (c, d) NM45-AN.

the green arrows), which seems to be related with dynamic crystallization. Dissimilarly, nanoscale precipitates decompose out from the BCC solid solution (Fig. 14c, d) in the ID region. Besides, dislocations can be pinned by precipitates, which inversely contributes to the multiplication of dislocations (see the blue arrows) and prevents the ID region from rapid softening after yielding.

4. Discussion

4.1. Effects of increasing Nb and Mo contents on dendrite segregation behavior

Fig. 5 shows that the increasing content of low T_m elements (Nb and Mo) can promote the dendrite segregation and formation of serrated GBs in NMx alloys, which mainly rests with solute effect. The existence of dendritic appearance means a change of grain growth from diffusion-controlled mode in NM5 alloy to dendrite tip radius- controlled mode in NM25 and NM45 alloys [33]. Dendrites initiate from the constitutional undercooling ahead of the growing interface, where solute effect dominates. The growth restriction factor Q is a key quantity to evaluate the influence of solute effect on grain growth and grain refinement, which is defined as [31].

$$Q = \left(\frac{\partial(\Delta T_{CS})}{\partial f_S}\right)_{f_S \to 0} = -\left(\frac{\partial T}{\partial f_S}\right)_{f_S \to 0} \quad (1)$$

here, $\Delta T_{CS} = T_L - T$ represents constitutional undercooling, i.e., the difference between liquidus temperature T_L and actual solidification temperature T. f_S is the solid fraction in mass percentage (wt%). T_L, T and f_S can be deduced from Fig. 4a. Q value equals to a factor b which can be obtained by fitting the ΔT_{CS}–f_S curve with a parabolic function $\Delta T_{CS} = a + b \cdot f_S + c \bullet f_S^2$ [34]. The calculated Q values are 39.0, 67.3 and 18.5 for NM5, NM25 and NM45 alloys, respectively. This means that the solute is Nb and Mo for NM5 while W and Ta for NM45 in a pseudo-binary NbMo-TaW system [31]. As NM5 alloy solidifies at the temperature between the T_m of W and Ta (~3400 K, Fig. 4a), only solvent element W is slightly undercooled in the liquid (while the solute elements not), which makes it difficult to induce constitutional undercooling in front of the growing interface. When NM25 alloy solidifies at the temperature of ~3100 K, which is slight below the melting temperature of Ta, an obvious segregation of W while a slight segregation of Ta (see Fig. 6b) occurs due to their different undercooling degree. The undercooling of W and Ta contributes to a severe constitutional undercooling ahead of the liquid front, which finally promotes the formation of dendritic structure and serrated GBs. Both solute elements (Ta and W) and the solvent element Mo are undercooled as NM45 alloy solidifies between the melting temperature of Nb and Mo (~2880 K), which leads to the pronounced elemental segregation as evident in Fig. 6b.

4.2. Effects of heterostructure on RT mechanical properties of NM45 alloy

The theoretical hardness (calculated based on the hardness of refractory elements using the rule-of-mixture) is 1.79 GPa and 1.50 GPa for NM25 and NM45 alloys, respectively, indicating that NM25 alloy should have higher hardness than NM45 alloy. However, NM25-AC and NM45-AC samples show almost the same hardness values (Fig. 8c, d). Considering their microstructure is almost the same (including grain size, serrated GBs, Ta—Nb rich oxides at GBs) except for the larger difference in hardness between DR and ID regions, the higher hardness of NM45-AC sample may come from the pronounced heterostructure.

NM45-AC sample is 257 MPa higher in yield strength at RT as compared with NM25-AC sample. The increment of yield strength ($\Delta\sigma_y$) generally depends on four strengthening mechanisms, which can be calculated by [35,36].

$$\Delta\sigma_y = \Delta\sigma_{ss} + \Delta\sigma_{gb} + \Delta\sigma_p + \Delta\sigma_d \quad (2)$$

Where σ_{ss}, σ_{gb}, σ_p, σ_d, represent the solid-solution strengthening, grain boundary strengthening, precipitation strengthening and dislocation strengthening, respectively. In this work, the contribution of precipitation and dislocation strengthening mechanisms to σ_y can be neglected due to no precipitate within the coarse grains (Fig. 5) and low dislocation density in the as-cast sample (Fig. 12b). The atomic size

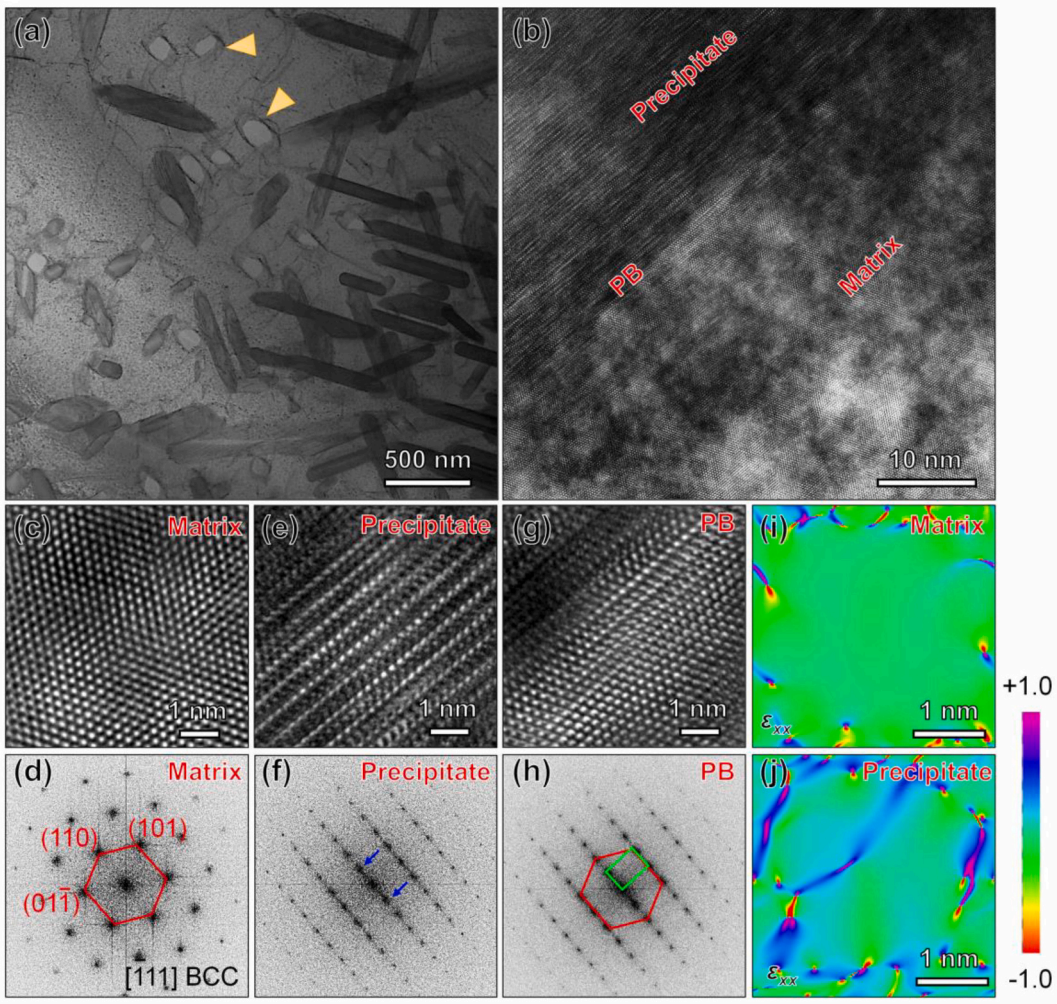

Fig. 11. **Fig. 11** TEM analysis of the precipitates in NM45-AN sample. (a) Bright field (BF) image; (b) HRTEM image at the PB; IFFT and FFT images of the (c, d) matrix, (e, f) precipitate and (g, h) PB; atomic strain distribution of the (i) matrix and (j) precipitate.

misfit is a widely used evaluator for solid-solution strengthening, which can be calculated by $\delta r_i = \frac{9}{8}\Sigma c_j \delta r_{ij}$ [37], where c_j is the atomic fraction of element j, $\delta r_{ij} = 2(r_i - r_j)/(r_i + r_j)$ indicates the atomic size difference between atoms i and j that calculated by their atomic size r_i and r_j. The calculated δr values are 0.0524 and 0.0556 for NM25 and NM45 alloys, respectively, which suggests that NM45 alloy exhibits comparable solid-solution strengthening as NM25 alloy. The effect of grain size on σ_y can be described by Hall-Petch relation [35] as

$$\sigma_{gb} = \sigma_0 + k_y \frac{1}{d^{1/2}} \tag{3}$$

where k_y is the Hall-Petch coefficient (1600 MPa $\mu m^{1/2}$ [38]) and the contribution of σ_{gb} to σ_y can be derived as $\Delta\sigma_{gb} = k_y\left(d_2^{-1/2} - d_1^{-1/2}\right)$ with the grain size of NM25 (d_1) and NM45 alloy (d_2). The calculated $\Delta\sigma_{gb}$ value is ~8 MPa, which is also neglectable. Moreover, the ID fraction of NM25 and NM45 alloy is 13% and 11% (measured by *ImageJ* software), respectively, suggesting the difference in ID fraction should have limited influence on the yield strength in this work. Thus, the increment in yield strength of NM45-AC sample is possibly attributed to the heterogeneous strengthening effect that arising from the dendritic heterostructure. The large RT plasticity of NM45-AC also benefits from the pronounced heterostructure, which mainly affected by both of the back stress and forward stress together with their interactions [32]. In addition, to further understand the improved plasticity of NM45 alloy, the single-crystal elastic constants (C11, C12, C44) were calculated by the first-principal calculation method (Table 3) to evaluate the intrinsic deformation ability. Meanwhile, the polycrystal-associated constants (including bulk moduli B, shear moduli G, Young's moduli E, as well as Poisson's ratio (v) and Pugh's ratio) were then deduced [39]. NM45 alloy has relatively smaller values for all elastic moduli together with larger values for v and Pugh's ratio, which evidences a better intrinsic plasticity in NM45 alloy [39].

4.3. Structural stability of NMx alloys at 1873 K

The presence of precipitates after annealing treatment indicates a low structural stability in the ID region of NM45 alloy at 1873 K. As mentioned in Fig. 6b, NM45-AC sample exhibits a severe dendrite segregation with high content of Nb and Mo, factually resulting in a significant discrepancy of the T_m in the DR and ID regions. The theoretical T_m can be calculated using the rule-of-mixture method [30] based on the specific composition in Fig. 6a. Thus, the annealing temperature 1873 K is $0.58T_m$ and $0.61T_m$ at the DR and ID regions, respectively, for NM25 alloy while $0.65T_m$ and $0.66T_m$ for NM45 alloy. $0.6T_m$ is generally considered as the upper limitation of service temperature [37]. It has been reported by P.K. Liaw that the ID region started to decompose after annealing at ~$0.55T_m$ for 7 days, and dendrites almost vanished after annealing at ~$0.6T_m$ for 7 days in light of the CrVNbMo RHEA [20]. For NbMoTaW RHEA, dendrites segregation was completely homogenized

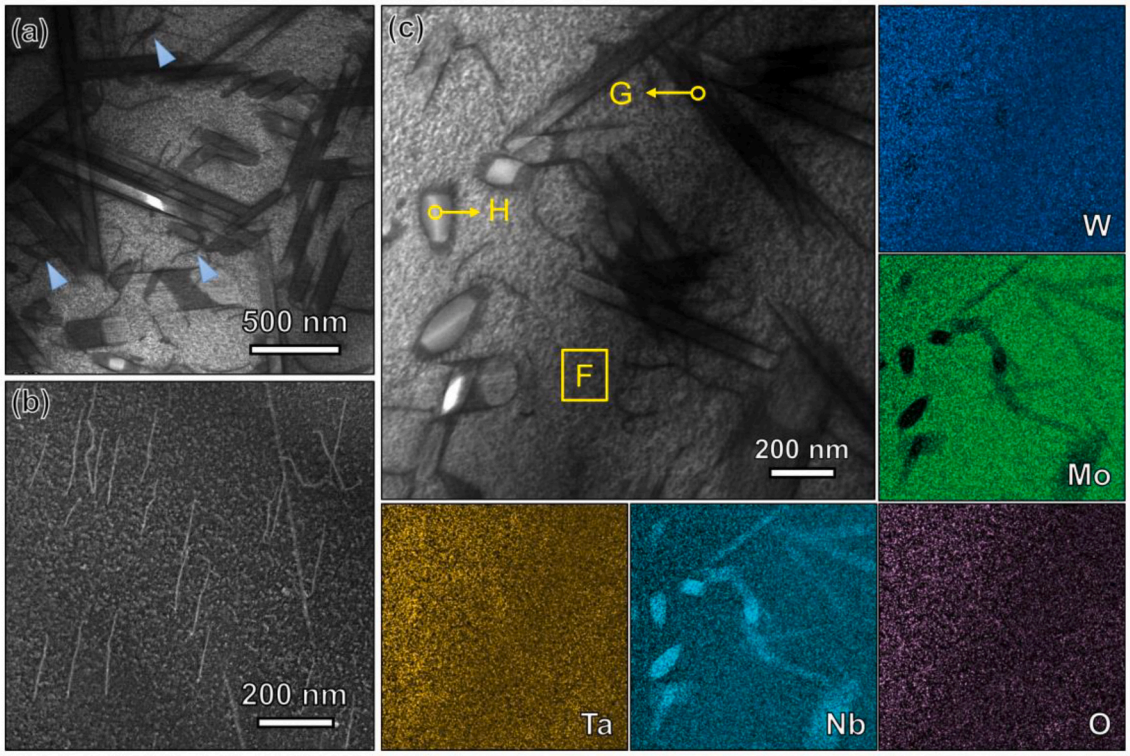

Fig. 12. **Fig. 12** Dislocations in (a) NM45-AN and (b)NM45-AC samples; (c) elemental distribution of the precipitates in NM45-AN sample.

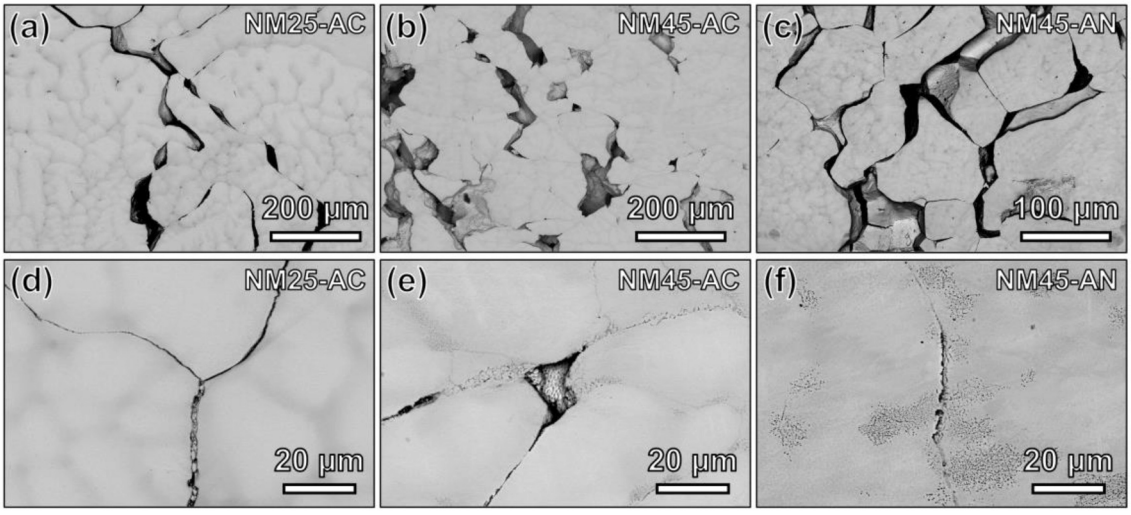

Fig. 13. **Fig. 13** BSE-SEM images from the cross-sectional view of NMx alloys after compression at 1873 K. (a, d) NM25-AC; (b, e) NM45-AC; (c, f) NM45-AN.

after annealing at ~0.65T_m for 7 days [40]. As elaborated above, a large amount of precipitation is reasonably present at the ID region of NM45-AN sample while NM25-AN sample remains almost stable. High content of W and Ta (with high T_m) also considerably contributes to the structural stability, as evidenced by the stable DR region in both NM25 and NM45 alloys (Fig. 10). Besides, nanoscale precipitates are also visible in the ID region of NM45-AC after deformation at 1873 K (Fig. 14c, d), revealing that the precipitation behavior is temperature-induced and stress-promoted.

4.4. The deformation behavior of NM45 alloy at 1873 K

Compared with the reported NbMoTaW RHEA by Senkov [7], NM45 alloy shows comparable yield strength even with a significantly reduced T_m (268 K). Particularly, NM45 alloy outperforms the previously reported RHEAs (with available yield strength at 1873 K) as considering its excellent specific yield strength as deformed at ~0.65T_m. This is related to its structural and compositional characteristics. When compressed at 1873 K, hetero-deformation occurs in NM45-AC sample, which is dominated by dislocation glide at the stable DR region while strengthened by nanoscale precipitates at the unstable ID region. Besides, the increasing content of Mo and Nb also endows NM45 alloy a high intrinsic strength. Modulus misfit is generally considered to be an indicator of excellent yield strength at high temperature [20], which can be calculated by $\delta G_i = \frac{9}{8}\Sigma G_j \delta G_{ij}$ [37], where G_j is the atomic fraction of element j, and $\delta G_{ij} = 2(G_i - G_j)/(G_i + G_j)$ indicates the modulus

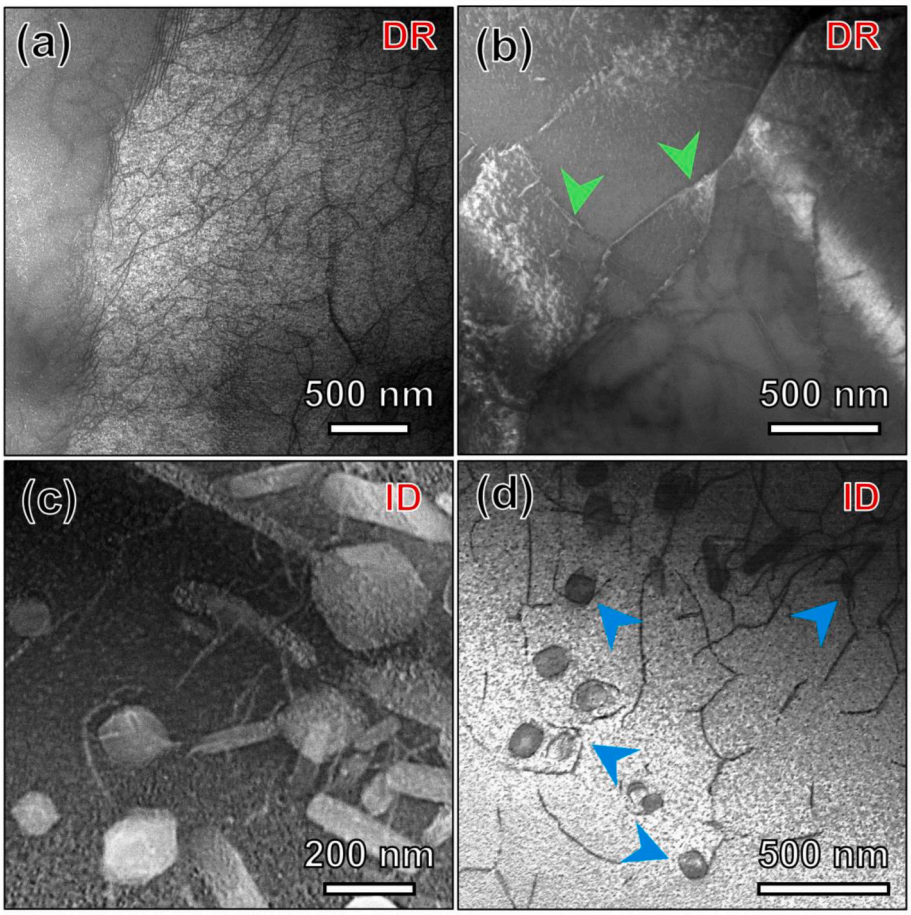

Fig. 14. **Fig. 14** TEM images in the (a, b) DR and (c, d) ID regions of NM45-AC sample after compression at 1873 K.

Table 3
Single-crystal elastic constants of NMx alloys that calculated by the first principal method.

Alloys	*C*11 (GPa)	*C*12 (GPa)	*C*44 (GPa)	*B* (GPa)	*G* (GPa)	*E* (GPa)	*v*	Pugh's ratio
NM25	385	162	76	236	89	237	0.333	2.655
NM45	377	142	58	222	74	200	0.349	2.987

difference between atoms *i* and *j* that calculated by their shear modulus G_i and G_j. The calculated δG values are 1.0109 and 1.4596 for NM25 and NM45 alloys, respectively, suggesting that NM45 alloy is more resistant to elastic deformation and therefore, should reach high yield strength. Note that, the yield strength of NM45 alloy is slightly lower (~57 MPa) than NM25 alloy at 1873 K in this work, which possible results from the higher homologous temperature of NM45 alloy. On one hand, the yield strength at 1873 K only reduced by 57 MPa as NM45 alloy deformed at a higher homologous temperature, suggesting that the enhanced heterogeneous microstructure by tuning dendrite segregation contributes to resisting early softening as strained at ultrahigh temperature. On the other hand, the slight reduction implies that the yield strength is more temperature-dependent at ultrahigh temperature. In other words, the breakthrough in ultrahigh-temperature yield strength without consideration of RT plasticity and material density may require the retention of moderate amounts of more refractory elements (like Ta, W) or further improvements in structural design, which may need to be investigated in future work.

All the NMx samples show an obvious strain softening behavior after peak stress at 1873 K (Fig. 1c), which presumably relates to dynamic recrystallization [41,42]. Direct evidence of the recrystallization-induced softening is the visible LAGBs at the DR region of NM45-AC alloy after compression at 1873 K (Fig. 14b). Material spallation from the side surface is another possible reason for the strain softening, which is similar with the reported NbMoTaW and VNbMoTaW RHEAs by Senkov [7]. Besides, coarse cracks, especially their propagation, can also result in stress reduction. Despite the presence of coarse cracks, no GB sliding occurs in any sample even at the testing temperature up to $0.66T_m$ for NM45 alloy, which greatly benefits from the heterostructure. Specifically, nanoscale precipitates formed at the ID region, significantly inhabiting rapid propagation of cracks (Fig. 13d–f). Moreover, both the as-cast and annealed NM45 samples exhibit a reduced softening rate, further demonstrating that softening can be restrained by the heterostructure (especially for the annealed sample with promoted precipitation behavior). The above analysis reveals that, to some extent, the NMx alloys experienced a sluggish disintegration at the strain softening stage before completely splitting apart.

Surface spallation also reveals that the primary mode is tensile rather than shear for the deformation of NMx samples at 1873 K [7], indicating NMx alloys cannot well resist localized tensile stress. Thus, Ta—Nb rich oxides are also possible to embrittle the GBs as deformed at 1873 K. Especially, NM45-AC sample displays a slow softening rate while its oxides contain less Ta than NM25-AC sample (Table S2). This is because the phase transition of Ta-oxides from an orthorhombic to a tetragonal

structure would occur at ~1800 K [43,44]. This transformation requires structural shrinkage and induces stress concentration, which makes GBs more susceptible to cracking under tensile stress. Notably, NM45-AC sample fractured at RT as strained >6% without intergranular failure, suggesting that in the current work, the segregation of O at GBs maybe not responsive to the intrinsic brittleness of NbMoTaW system RHEAs. Nevertheless, removing GB oxides may help to obtain more stable mechanical properties at high temperature.

5. Conclusions

$Nb_{45}Mo_{45}Ta_5W_5$ (NM45) RHEA was designed on a heterostructure strategy by tuning dendrite segregation to promote the synergy of RT plasticity and HT strength. Pronounced heterostructure contributes to a large RT plasticity of 6.1% and a high yield strength of 440 MPa at 1873 K in the as-cast NM45 sample. After annealing treatment, nanoscale ordered precipitates decompose out from the BCC matrix at the interdendrite region, which further increases the RT plasticity to 9.0% while slightly decreases the yield strength to 415 MPa at 1873 K. Heterodeformation appears as the as-cast NM45 alloy deformed at 1873 K, where dominated by dislocation glide in the stable DR region while strengthened by nanoscale precipitates in the unstable ID region. The strength retention up to 1873 K of NM45 alloy arises from the pronounced heterostructure and the large modulus misfit. In this work, the dendritic heterostructure strategy provide a feasible method to toughen brittle RHEAs and paves the way to design NbMoTaW system RHEAs with high HT strength in combination of large RT plasticity.

CRediT authorship contribution statement

Bo Sun: Conceptualization, Methodology, Investigation, Writing – original draft, Writing – review & editing. **Qianqian Wang:** Writing – review & editing, Funding acquisition. **Jinyong Mo:** Investigation. **Bingjie Wang:** Investigation. **Xiubing Liang:** Resources, Supervision. **Baolong Shen:** Funding acquisition, Project administration, Supervision.

Declaration of Competing Interest

The authors declare that they have no known competing financial interests or personal relationships that could have appeared to influence the work reported in this paper.

Data availability

Data will be made available on request.

Acknowledgements

This work was supported by the Key Research and Development Program of Jiangsu Province (Grant No. BE2021088), the Fundamental Research Funds for the Central Universities (Grant No. 2242023K40029), and the open research fund of Jiangsu Key Laboratory for Advanced Metallic Materials, Southeast University (Grant No. AMM2023B05).

Appendix A. Supplementary data

Supplementary data to this article can be found online at https://doi.org/10.1016/j.ijrmhm.2023.106469.

References

[1] D.B. Miracle, O.N. Senkov, A critical review of high entropy alloys and related concepts, Acta Mater. 122 (2017) 448–511.
[2] W. Xiong, A.X.Y. Guo, S. Zhan, et al., Refractory high-entropy alloys: a focused review of preparation methods and properties, J. Mater. Sci. Technol. 142 (2023) 196–215.
[3] P. Tsakiropoulos, Alloys for application at ultra-high temperatures: Nb-silicide in situ composites; challenges, breakthroughs and opportunities, Prog. Mater. Sci. 123 (2022), 100714.
[4] J. Yeh, Recent progress in high-entropy alloys, Ann. Chim. Sci. Mater. 31 (2006) 633–648.
[5] K.Y. Tsai, M.H. Tsai, J.W. Yeh, Sluggish diffusion in Co-Cr-Fe-Mn-Ni high-entropy alloys, Acta Mater. 61 (2013) 4887–4897.
[6] O.N. Senkov, G.B. Wilks, D.B. Miracle, et al., Refractory high-entropy alloys, Intermetallics 18 (2010) 1758–1765.
[7] O.N. Senkov, G.B. Wilks, J.M. Scott, et al., Mechanical properties of $Nb_{25}Mo_{25}Ta_{25}W_{25}$ and $V_{20}Nb_{20}Mo_{20}Ta_{20}W_{20}$ refractory high entropy alloys, Intermetallics 19 (2011) 698–706.
[8] Y. Zou, H. Ma, R. Spolenak, Ultrastrong ductile and stable high-entropy alloys at small scales, Nat. Commun. 6 (2015) 7748.
[9] J. Zhou, Y. Cheng, Y. Chen, et al., Composition design and preparation process of refractory high-entropy alloys: a review, Int. J. Refract. Met. H. 105 (2022), 105836.
[10] C.H. Belcher, B.E. MacDonald, D. Apelian, et al., The role of interstitial constituents in refractory complex concentrated alloys, Prog. Mater. Sci. 137 (2023), 101140.
[11] O.N. Senkov, D.B. Miracle, K.J. Chaput, et al., Development and exploration of refractory high entropy alloys—a review, J. Mater. Res. 33 (2018) 3092–3128.
[12] Z. Wang, S. Chen, S. Yang, et al., Light-weight refractory high-entropy alloys: a comprehensive review, J. Mater. Sci. Technol. 151 (2023) 41–65.
[13] Y. Wan, X. Wang, Z. Zhang, et al., Structures and properties of the $(NbMoTaW)_{100-x}C_x$ high-entropy composites, J. Alloy. Compd. 889 (2021), 161645.
[14] Z.D. Han, N. Chen, S.F. Zhao, et al., Effect of Ti additions on mechanical properties of NbMoTaW and VNbMoTaW refractory high entropy alloys, Intermetallics 84 (2017) 153–157.
[15] Y. Wan, J. Mo, X. Wang, et al., Mechanical properties and phase stability of WTaMoNbTi refractory high-entropy alloy at elevated temperatures, Acta Metall. Sini–Engl. 34 (2021) 1585–1590.
[16] Q. Wei, G. Luo, J. Zhang, et al., Effect of raw material forms on the microstructure and mechanical properties of $MoNbRe_{0.5}TaW$ high-entropy alloy, Mat. Sci. Eng. A 794 (2020), 139632.
[17] Q. Wei, Q. Shen, J. Zhang, et al., Microstructure and mechanical property of a novel ReMoTaW high-entropy alloy with high density, Int. J. Refract. Met. H. 77 (2018) 8–11.
[18] Y. Wan, Q. Wang, J. Mo, et al., WReTaMo refractory high-entropy alloy with high strength at 1600 °C, Adv. Eng. Mater. 24 (2022) 2100765.
[19] M. Moorehead, K. Bertsch, M. Niezgoda, et al., High-throughput synthesis of Mo-Nb-Ta-W high-entropy alloys via additive manufacturing, Mater. Design 187 (2020), 108358.
[20] R. Feng, B. Feng, M.C. Gao, et al., Superior high-temperature strength in a supersaturated refractory high-entropy alloy, Adv. Mater. 33 (2021) 2102401.
[21] T. Li, W. Jiao, J. Miao, et al., A novel ZrNbMoTaW refractory high-entropy alloy with in-situ forming heterogeneous structure, Mat. Sci. Eng. A 827 (2021), 142061.
[22] T.R. Middya, A.N. Basu, S. Sengupta, Self-consistent *T*-matrix solution for the effective elastic properties of perfectly disordered multiphase solids, J. Appl. Phys. 58 (1985) 1809–1813.
[23] H. Mao, H. Chen, Q. Chen, TCHEA1: a thermodynamic database not limited for "high entropy" alloys, J. Phase Equilib. Diff. 38 (2017) 353–368.
[24] G. Kresse, J. Furthmuller, Efficient iterative schemes for ab initio total-energy calculations using a plane-wave basis set, Phys. Rev. B 54 (1996) 11169–11186.
[25] P.E. Blochl, Projector augmented-wave method, Phys. Rev. B 50 (1994) 17953–17979.
[26] A. van de Walle, P. Tiwary, M. de Jong, et al., Efficient stochastic generation of special quasirandom structures, Calphad 42 (2013) 13–18.
[27] J. Mo, X. Liang, B. Shen, et al., Local lattice distortions, phase stability, and mechanical properties of NbMoTaWHfx alloys: a combined theoretical and experimental study, Comput. Mater. Sci. 217 (2023), 111891.
[28] O.N. Senkov, T.I. Daboiku, T.M. Butler, et al., High-temperature mechanical properties and oxidation behavior of Hf-27Ta and Hf-21Ta-21X (X is Nb, Mo or W) alloys, Int. J. Refract. Met. H. 96 (2021), 105467.
[29] Z. Wang, H. Wu, Y. Wu, et al., Solving oxygen embrittlement of refractory high-entropy alloy via grain boundary engineering, Mater. Today 54 (2022) 83–89.
[30] L. Vegard, The constitution of mixed crystals and the space occupied by atoms, Zeitschrift Fur Physik 5 (1921) 17–26.
[31] M. Wang, Z.L. Ma, Z.Q. Xu, et al., Designing $V_xNbMoTa$ refractory high-entropy alloys with improved properties for high-temperature applications, Scripta Mater. 191 (2021) 131–136.
[32] Y. Zhu, X. Wu, Heterostructured materials, Prog. Mater. Sci. 131 (2023), 101019.
[33] M. Easton, D. Stjohn, Grain refinement of aluminum alloys: part I. The nucleant and solute paradigms : a review of the literature, Metall. Mater. Trans. A 30 (1999) 1613–1623.
[34] R. Schmid-Fetzer, A. Kozlov, Thermodynamic aspects of grain growth restriction in multicomponent alloy solidification, Acta Mater. 59 (2011) 6133–6144.
[35] F. He, D. Chen, B. Han, et al., Design of $D0_{22}$ superlattice with superior strengthening effect in high entropy alloys, Acta Mater. 167 (2019) 275–286.
[36] B. Wang, Q. Wang, N. Lu, et al., Enhanced high-temperature strength of HfNbTaTiZrV refractory high-entropy alloy via Al_2O_3 reinforcement, J. Mater. Sci. Technol. 123 (2022) 191–200.

[37] O.N. Senkov, J.M. Scott, S.V. Senkova, et al., Microstructure and room temperature properties of a high-entropy TaNbHfZrTi alloy, J. Alloy. Compd. 509 (2011) 6043–6048.
[38] B. Kang, J. Lee, H.J. Ryu, et al., Ultra-high strength WNbMoTaV high-entropy alloys with fine grain structure fabricated by powder metallurgical process, Mat. Sci. Eng. A 712 (2018) 616–624.
[39] J. Mo, Y. Wan, Z. Zhang, et al., First-principle prediction of structural and mechanical properties in $NbMoTaWRe_x$ refractory high-entropy alloys with experimental validation, Rare Metals 41 (2022) 3343–3350.
[40] Y. Zou, S. Maiti, W. Steurer, et al., Size-dependent plasticity in an $Nb_{25}Mo_{25}Ta_{25}W_{25}$ refractory high-entropy alloy, Acta Mater. 65 (2014) 85–97.
[41] R.R. Eleti, T. Bhattacharjee, A. Shibata, et al., Unique deformation behavior and microstructure evolution in high temperature processing of HfNbTaTiZr refractory high entropy alloy, Acta Mater. 171 (2019) 132–145.
[42] R.R. Eleti, A.H. Chokshi, A. Shibata, et al., Unique high-temperature deformation dominated by grain boundary sliding in heterogeneous necklace structure formed by dynamic recrystallization in HfNbTaTiZr BCC refractory high entropy alloy, Acta Mater. 183 (2020) 64–77.
[43] Y. Yang, Y. Kawazoe, Prediction of new ground state crystal structure of Ta_2O_5, Phys. Rev. Mater. 2 (2018), 034602.
[44] K.T. Jacob, C. Shekhar, Y. Waseda, An update on the thermodynamics of Ta_2O_5, J. Chem. Thermodyn. 41 (2009) 748–753.